ACS APPLIED MATERIALS & INTERFACES

www.acsami.org

Research Article

Accelerated Growth of Electrically Isolated Lithium Metal during Battery Cycling

Yibo Zhao,[‡] Yifan Wu,[‡] Huihui Liu, Sung-Liang Chen, and Shou-Hang Bo*

Cite This: *ACS Appl. Mater. Interfaces* 2021, 13, 35750−35758

Read Online

ACCESS | Metrics & More | Article Recommendations | Supporting Information

ABSTRACT: Severe capacity loss during cycling of lithium-metal batteries is one of the most concerning obstacles hindering their practical application. As this capacity loss is related to the variety of side reactions occurring to lithium metal, identification and quantification of these lithium-loss processes are extremely important. In this work, we systematically distinguish and quantify the different rates of lithium loss associated with galvanic corrosion, the formation of a solid−electrolyte interphase, and the formation of electrically isolated lithium metal (i.e., "dead" lithium). We show that the formation of "dead" Li is accelerated upon cycling, dominating the total lithium loss, with much slower rates of lithium loss associated with galvanic corrosion and formation of the solid−electrolyte interphase. Furthermore, photoacoustic imaging reveals that the three-dimensional spatial distribution of "dead" Li is distinctly different from that of freshly deposited lithium. This quantification is further extended to a solid-state Li/Cu cell based on a $Li_{10}GeP_2S_{12}$ solid-state electrolyte. The lithium loss in the solid-state cell is much severer than that of a conventional lithium-metal battery based on a liquid electrolyte. Our work highlights the importance of quantitative studies on conventional and solid-state lithium-metal batteries and provides a strong basis for the optimization of lithium-metal electrochemistry.

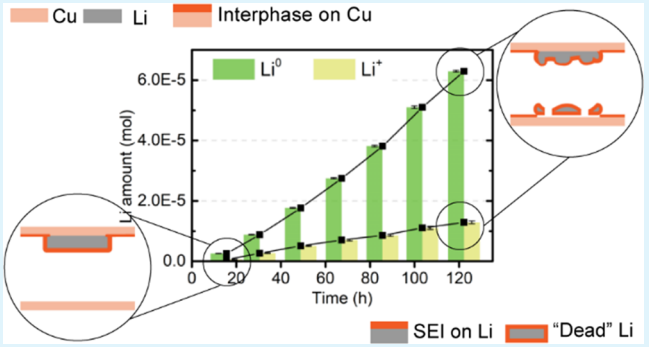

KEYWORDS: *electrically isolated lithium, lithium-metal battery, lithium-loss rate, gas chromatography, photoacoustic imaging*

INTRODUCTION

With the increasing demand for more energy-dense energy storage systems, lithium-metal batteries have been brought back to the main stage. The theoretical capacity of lithium metal is 3860 mA h g^{-1}, which is 10 times higher than that of a graphite anode. Therefore, lithium metal is expected to play an essential role in the next-generation batteries with substantially increased energy density.[1,2] The recent development of anode-free cells can further increase the energy density but places even more stringent requirements on the stable cycling of lithium-metal anodes.[3]

The capacity loss associated with lithium-metal cycling is significant and, when combined with safety issues, greatly limits the application of lithium-metal anodes in practical cells. To meet the commercial use requirements for electric vehicles, lithium-ion batteries need to achieve 80 or 90% capacity retention for over 1000 cycles or 500 cycles, respectively (according to GB/T 31484-2015, National Standard of the People's Republic of China).[4] For a lithium-metal battery with 80% capacity remaining after 1000 cycles, an average Coulombic efficiency (CE) of 99.9% is needed, when 80% lithium-metal excess is applied.[5] However, state-of-the-art Li-metal batteries can only achieve an average CE of 99.8% for several tens of cycles and may experience sudden "death" when operated for an extended time.[2,6−8] A 0.1% difference in the CE can result in a large difference in the cycle life.[5,9] Anode-free Li-metal batteries experience more acute capacity loss during cycling (down to 80% within a few tens of cycles).[10] It is therefore extremely important to identify the processes that cause Li loss and to quantify the rate of these loss processes with high precision for the development of scientific and engineering approaches to optimize Li-metal electrochemistry.

The capacity loss processes in Li-metal batteries are complicated.[11,12] Solid−electrolyte interphase (SEI) formation, galvanic corrosion, and the formation of electrically isolated lithium metal (also called "dead" Li) all cause Li loss. In the following discussion, we use Li^+ and Li^0 loss to denote the formation of Li^+-containing decomposition products (such as LiF and Li_2O in the SEI formation and/or galvanic corrosion processes) and the formation of electrochemically inactive Li metal ("dead" Li), respectively.[13−19]

Received: May 14, 2021
Accepted: July 10, 2021
Published: July 21, 2021

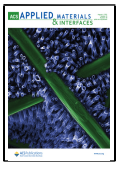

https://doi.org/10.1021/acsami.1c08944
ACS Appl. Mater. Interfaces 2021, 13, 35750−35758

SEI formation and galvanic corrosion are two important Li^+-loss processes. SEI formation starts immediately when highly reactive lithium metal is immersed in a liquid electrolyte, producing reductive decomposition products of the liquid electrolyte.[20−23] The SEI blocks electrons and limits ion transport to the Li metal, increasing the charge-transfer resistance associated with the Li^+/Li redox reaction. The morphology and composition of the SEI also significantly affect the deposition morphology of lithium metal.[20,24−28] A widely accepted model for SEI growth between alkali metals and nonaqueous electrolytes was proposed by Peled in 1979.[21] The growth of the SEI thickness (L_{SEI}) with respect to time (t) follows a power law as $L_{SEI} \propto t^{\beta}$ (including both rest and battery cycling time periods), where β typically ranges between 0.2 and 0.5. However, recent works using cryogenic electron microscopy (cryo-EM) have revealed the layered/mosaic structures of the SEI, indicating that the growth of the SEI layer is a rather complex process.[29−31]

Galvanic corrosion occurs when two dissimilar metals are in contact, e.g., the Li-metal anode and the Cu current collector, in the presence of a liquid electrolyte.[17,18] During the corrosion process, Li metal is oxidized to Li^+, releasing electrons through the Cu current collector, where the liquid electrolyte gets reduced, forming a Li^+-containing layer on the Cu surface. The zero resistance ammetry (ZRA) method can be used to measure galvanic corrosion current density between two metals.[32,33] The galvanic corrosion current density of Li/Cu cells was previously observed to be approximately 0.1−0.2 μA cm^{-2} for cells with a rest period of 100 h.[17,18]

"Dead" Li forms when metallic Li becomes electrically isolated, during the stripping and plating processes. Although the formation of "dead" Li does not directly affect the charge-transfer resistance associated with the Li^+/Li redox reaction, it can consume the liquid electrolyte if the fresh Li-metal surface is exposed. Both galvanic corrosion and SEI growth can lead to "dead" Li formation.[18,20] 2D techniques, e.g., operando optical imaging and battery thickness measurements were used to probe "dead" Li.[34−37] Spectroscopically, the pioneering work from Fang et al. introduced titration gas chromatography (TGC) into "dead" Li quantification. They identified "dead" Li formation as the primary source of Li loss.[38] This method was also applied to quantify different decomposition products on battery anode surfaces.[39−41] ^{7}Li nuclear magnetic resonance (NMR) spectroscopy is another powerful tool for the quantification of "dead" Li.[42−44] These NMR and TGC studies suggest that the contribution of "dead" Li formation to the total capacity/Li loss varies with the electrolyte composition, current density, and structure of the current collector.

In this work, we combined gas chromatography (GC) and electrochemical cycling with impedance spectroscopy to systematically distinguish and measure the rates of the Li^+ and Li^0 loss processes in $LiPF_6$-carbonate liquid-electrolyte Li/Cu cells, where Li^+ loss was resulted from SEI formation and galvanic corrosion and Li^0 loss was resulted from "dead" Li formation. The rates of these Li loss processes are currently not available in the literature, which are, however, extremely important to battery life prognosis and which determine the long-term cycling performance of Li-metal batteries. In this work, the growth of "dead" Li was observed to accelerate as cycling proceeded, whereas the rate of Li^+ loss remained almost constant and was much slower. Furthermore, we employed photoacoustic (PA) imaging for 3D visualization of the "dead" Li on the Cu surface after extended cycling. The morphology of "dead" Li was revealed to be distinctly different from that of freshly deposited Li. Our previous works demonstrated the feasibility of using PA imaging for 3D visualization of Li metal with high temporal resolution and high sensitivity at the micrometer scale.[45,46] Finally, we applied a similar quantification method on a Li/Cu solid-state cell with a $Li_{10}GeP_2S_{12}$ (LGPS) solid-state electrolyte. More than 99% of the Li loss was tied to the interphase formation, in stark contrast to that in a similar cell with a $LiPF_6$-carbonate liquid electrolyte.

EXPERIMENTAL SECTION

Cell Preparation and Cycling. Lithium-metal foils (Oujin, Shanghai, 5 mm diameter, 300 μm thickness) were used as the lithium source and anode material. Thick Cu pellets (10 mm diameter, 1 mm thickness) were used as both negative and positive current collectors. Celgard 2500 (25 μm) was used as a separator. $LiPF_6$ (1 M) in ethylene carbonate (EC):diethyl carbonate (DEC):dimethyl carbonate (DMC) (1:1:1 volume ratio, Sinopoly, China, 120 μL) was used in each cell. The stacked cell components were sealed in coin cells (CR2025). Assembly of the cells was conducted in an argon-filled glovebox (Mikrouna, O_2 and H_2O < 0.1 ppm). Galvanostatic cycling with a current density of 1 mA cm^{-2} (0.196 mA) was performed for all the cells. The discharge time was 2 h, and the cutoff voltage was set to ±1 V. Electrochemistry measurements were performed using a Neware battery test system. For the solid-state cells, Li/Cu half-cells were assembled layer-by-layer in a sequence of Cu pellets (10 mm diameter, 1 mm thickness), the $Li_{10}GeP_2S_{12}$ solid-state electrolyte (10 mm diameter, 1.4 mm thickness, Kejing, MTI), and lithium-metal foils (7 mm diameter, China Energy Lithium) in an EQ-PSC-type pressure-controlled split coin cell (Kejing, MTI). Solid-state electrolyte pellets were prepared by cold pressing with a uniaxial pressure of 4 tons in a 10 mm stainless-steel die. Assembly of the solid-state cells was conducted in an argon-filled glovebox (Mikrouna, O_2 and H_2O < 0.1 ppm). A current of 0.100 mA (current density of 1.3 mA cm^{-2}) was selected for galvanostatic cycling with cutoff voltages of ±1 V. Electrochemistry measurements were conducted on the same equipment as the cells with the liquid electrolyte.

GC Measurements. The cells after cycling were disassembled in a glovebox. The Cu current collectors on the positive side and separators were collected from the cells. The current collectors and separators were transferred into flasks (~80 or ~140 mL), which were sealed with rubber stoppers. An excess amount of deionized water (2 mL) was injected into the flask in each titration. After a full reaction, 1 mL of gas was extracted from the flask and injected into the GC instrument (GC-14B, Shimadzu). The retention time from 0 to 2 min was recorded to reveal the H_2 and air peaks. The concentrations of H_2 in the flasks were determined by comparing the peak areas at ~0.75 min with calibrations from standard H_2 gas. For the solid-state cells, the Cu current collectors were collected after cycling and sealed in 20 mL headspace vials for GC measurements. An excess amount of deionized water (5 mL) was injected into the headspace vials in each titration. 1 mL of gas was extracted from the vials and injected into the GC instrument using the same approach as that used for the liquid-electrolyte cells. The concentrations of H_2 within the vials after titration were determined after recording, calibration, and integration.

PA Imaging. PA imaging is a noninvasive and high-resolution 3D imaging technique that reveals the intrinsic contrast in the local optical absorption coefficients of a sample.[47] During PA imaging, pulsed light is typically excited on the sample to induce acoustic waves, which are then detected and transformed into electrical signals to form images. In particular, the time of flight (ToF) of the detected acoustic waves can provide height-resolved information, thus enabling morphological observation. In the experiment, the Li/Cu cell after 45 cycles was disassembled, and the positive Cu current collector with "dead" Li on the surface was sealed inside a polyethylene plastic bag with liquid electrolyte inside as a coupling agent. The sample was then

https://doi.org/10.1021/acsami.1c08944
ACS Appl. Mater. Interfaces 2021, 13, 35750−35758

stuck to the sample stage for scanning. A home-built probe-based PA microscope (Figures S6 and S7) with a lateral resolution of ~3.15 μm (Figure S8) and an axial resolution of ~28.5 μm (Figure S9) was used to acquire PA images. Pulsed laser light (532 nm) with a pulse energy of ~73 nJ (to avoid damage to the Li metal by excitation light) was focused on the sample to excite PA signals.[46] A PA image of a 10 × 10 mm^2 region was acquired to include the entire current collector surface. With a voxel size of 8 × 8 × 7.4 μm^3, the imaging process took ~70 min.

EIS Measurement. EIS measurements were conducted on a Biologic SP-200. The polarization voltage was set to 10 mV over the open-circuit voltage, and the frequency range was set to 7 MHz to 0.1 Hz. The impedance data were fitted with Zview. Only the semicircle in the intermediate frequency region was analyzed, which represents the impedance of the interphase layer.

RESULTS

Accelerated Accumulated Li Loss. In a Li/Cu half-cell cycling experiment, we first moved lithium ions from the lithium metal to the Cu current collector under a current density of 1 mA cm^{-2} (0.196 mA) for 2 h. Then, by switching the direction of the current, the deposited Li metal was stripped from the Cu surface and was plated back on the lithium-metal surface. The CE of this cycling process is the ratio of the charge duration (less than 2 h) to the discharge duration (2 h)

$$\mathrm{CE} = \frac{Q_{\mathrm{charge}}}{Q_{\mathrm{discharge}}} = \frac{t_{\mathrm{charge}}}{t_{\mathrm{discharge}}}$$

We prepared 7 cells, which were cycled for either 1, 5, 10, 15, 20, 25, or 30 cycles. These cells were used in the GC analysis, as will be discussed below. The charge and discharge curves of these cells are presented in Figure S1. An excess amount of Li metal was used (with a total areal capacity of approximately 60 mA h cm^{-2} for a 300 μm lithium foil), ensuring 2 mA h cm^{-2} of lithium deposition for each cycle. However, not all the lithium could be stripped back in the subsequent charging, resulting in a sudden increase in the voltage, reaching a cutoff voltage of 1 V. The cells showed similar CE changes over cycles (as shown in Figure S2). Despite the CE fluctuation in the first cycle, the CEs of all the cells first increased to approximately 85% followed by a decrease in the CE and were finally stabilized at approximately 80%. In Figure 1, the CE for the cell cycled 30 times is shown on the left y-axis. For each cycle, 15 to 20% CE loss was observed. These CE losses are the combined result of galvanic corrosion, SEI formation, and electrically isolated lithium-metal formation on the Cu and lithium-metal surface, as discussed above.

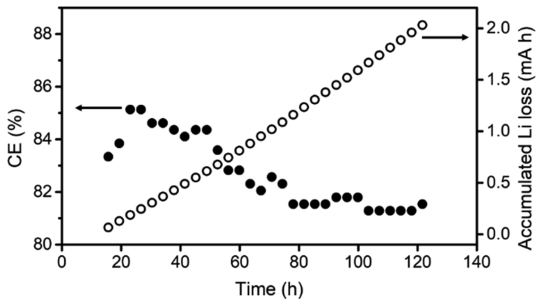

Figure 1. CE and accumulated Li loss (in mA h) of the Li/Cu cell cycled for 30 cycles.

The accumulated Li loss in terms of mA h for the 30-cycle cell was calculated after each cycle and is plotted versus time in Figure 1 (right y-axis). According to previous analysis on capacity loss in Li-ion batteries, the accumulated capacity loss follows a power function law.[48,49] In our experiments, we observed that the power function fitting, $\sum\Delta Q = at^{\beta}$, where $\sum\Delta Q$ is the accumulated Li loss, a is a constant, t is time, and β is a scaling factor, fitted well with the experimental data (R^2 = 0.99). For this Li/Cu cell, the scaling factor β was calculated to be 1.33 (see Figure S3 for the fitting curve and fitting parameters). This result indicates that in Li-metal or anode-free batteries for a longer cycle time, the accumulated capacity loss, or Li loss, is accelerated, different from that of Li-ion batteries, where carbon was used as the anode (the experimental and modeling scaling factors were all less than 1).[12,48,49] We will discuss the origin of this accelerated accumulated capacity loss in the following section.

Accelerated Li^0 Loss. GC measurements were used to quantify the Li loss in the form of "dead" lithium formation (denoted as Li^0 loss) as a function of time. The analysis of GC data follows the reaction

$$2\mathrm{Li} + \mathrm{H_2O} \rightarrow 2\mathrm{LiOH} + \mathrm{H_2}\uparrow$$

The Cu current collector was collected after one or several full cycles. Then, an excess amount of water was used to react with the "dead" lithium metal that could not be stripped from the Cu current collectors. By measuring the gas concentration of H_2 in the reaction, the amount of metallic Li was calculated according to the ideal gas equation and the stoichiometry of the reaction presented above. By the time of submission of the current work, we noticed an X-ray diffraction study of SEI components formed on the Li-metal surface in Li/Cu cells.[50] This work suggested the presence of crystalline LiH in the SEI of the Li-metal anode. Therefore, a small amount of LiH might also be present in our cells. Because the reaction of LiH with water also produces H_2 gas, the actual amount of "dead" Li can be smaller due to the possible existence of LiH. Therefore, the absolute amount of "dead" Li derived in our work should be considered as an upper bound. The GC profile is plotted as a function of retention time in Figure 2a. The peaks with a retention time of ~0.75 min, shaded in blue, correspond to H_2. The other peaks located at a retention time of approximately 1.45 min indicate the presence of air, corresponding to the remanent air in the needle of the syringe used in the measurements. The separators from these cells were also tested by GC, which revealed that the Li loss in separators (stemming from the sample preparation or lithium protrusions in the separator) did not affect the accuracy of the GC results. The amount of produced H_2 from the reaction with "dead" Li on the Cu surface (left figure in Figure 2a) was much larger than that from the separators (inset figure in Figure 2a). The derived amount of metallic Li detected in the separators was less than 1% of that on the Cu surfaces (Table S1). Thus, in this work, the Li loss in the separators is neglected. However, it is intriguing to note that such a limited amount of Li loss in the separators can in fact short-circuit Li-metal batteries. Once the amount of "dead" Li (or Li^0 loss) is known, the Li^+ loss can be determined by subtracting the amount of Li^0 loss from the total Li loss, where the total Li loss is calculated by adding up the losses in capacities (in mA h) for every cycle.

The rates of capacity loss in the form of "dead" Li and in the form of Li^+ through parasitic reactions were then measured, which revealed that the Li^0 loss rate accelerated while the rate

https://doi.org/10.1021/acsami.1c08944
ACS Appl. Mater. Interfaces 2021, 13, 35750−35758

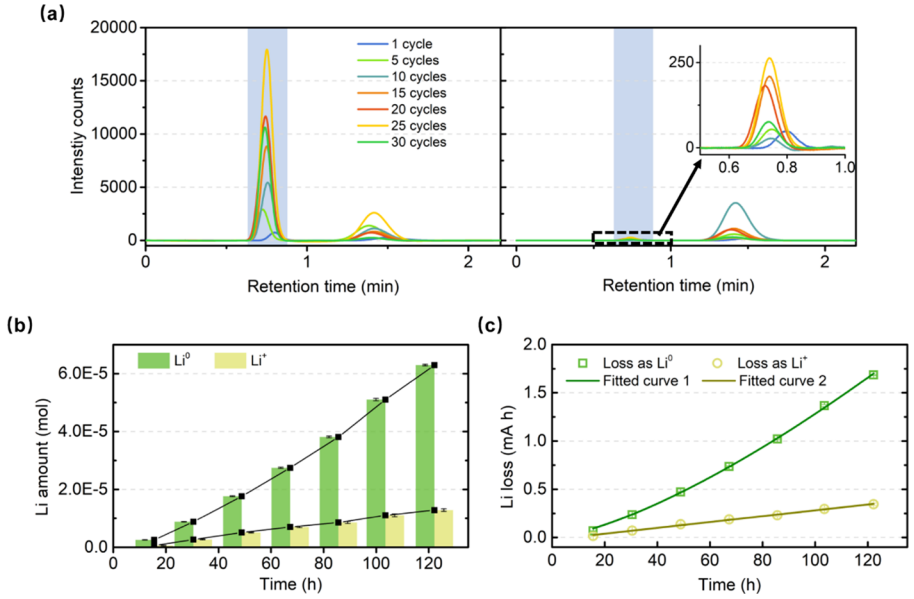

Figure 2. (a) GC profile of water titration experiments for Cu current collectors (left) and separators (right) of the cells that were cycled for 1, 5, 10, 15, 20, 25, and 30 times. The peaks at a retention time of ~0.75 min correspond to detected H_2 (shaded in blue). The inset presents an enlarged view of the black-dashed region. (b) Li amount (in mol) contributed by Li^0 and by Li^+ (obtained by subtracting the Li^0 loss from the total Li loss obtained from electrochemistry) with respect to time. (c) Li^0 and Li^+ loss in mA h. The former is fitted by a power function (fitted curve 1), and the latter is fitted by a linear function (fitted curve 2).

of total Li^+ loss remained unchanged in the first 30 cycles. Figure 2b shows the Li loss contributions (in mol) from Li^0, resulting from "dead" Li formation, and from Li^+ (from SEI formation and corrosion) for the cells after 1, 5, 10, 15, 20, 25, and 30 cycles. "Dead" Li formation contributed to more than 75% of the total Li loss for all the cells, as shown in Table 1.

Table 1. Percentages of Li^0 and Li^+ of the Total Li Loss

cycle number	Li^0 (%)	Li^+ (%)
1	81.15	18.85
5	76.84	23.16
10	77.60	22.40
15	79.62	20.38
20	81.65	18.35
25	82.21	17.79
30	83.02	16.98

The rates of Li^0 and Li^+ losses were extracted by fitting the data in Figure 2c. A power function ($\sum\Delta Q = at^{\beta}$) fitted the growth of "dead" Li well with an R^2 of 0.99. This finding is consistent with Peled's model albeit with a much larger scaling factor β of 1.41.[21] However, for Li^+, a linear function fits better than a power function (R^2 of 0.99). The Li^+ loss rate was calculated to be 0.00304 mA. This result indicates that 1.55% of the 0.196 mA Faradic current during charging and discharging was constantly wasted by the Li^+ loss. The fitting parameters are listed in Table 2, and the fitted curves are presented in Figure 2c. We note that the scaling factor of the power function fitting for Li^0 was very close to that for the accumulated Li loss (1.41 vs 1.33). However, the growth rate of Li^+ was much lower, in particular after extended cycling. These results suggest that the accelerated growth of the accumulated Li loss is dominated by the accelerated "dead" Li formation.

3D Spatial Distribution of "Dead" Li. We compared the spatial distribution of freshly deposited Li with that of "dead"

Table 2. Fitting Parameters for the Power Function of the Amount of Li^0 Loss and for the Linear Function of the Amount of Li^+ Loss

	fitted curve 1		fitted curve 2
a	0.00193	intercept	−0.02238
β	1.41	slope	0.00304
R^2	0.99	R^2	0.99

Li to determine if the "dead" Li showed any particular growth pattern on the Cu current collector. In our previous work, we examined the surface of freshly deposited lithium (~10 mA h cm^{-2}) using PA imaging.[46] The freshly deposited lithium had an average height of ~44.35 μm with a relatively smooth surface in the center. In this work, the 3D spatial distribution of "dead" Li on the Cu current collector surface after 45 cycles was investigated using PA imaging. Using the power function developed in the previous section, the amount of "dead" Li was estimated to be close to 10 mA h cm^{-2}. A schematic illustration of a sample under PA imaging is presented in Figure 3a. Imaging was performed by scanning on the $x-y$ plane. The height-encoded map of the current collector surface is displayed in Figure 3b. This figure presents the relative height of "dead" Li with respect to the lowest point on the current collector surface, which is also the reference height (i.e., height of 0 μm in Figure 3b). The (absolute) height distribution of "dead" Li was then calculated by point-to-point subtracting the surface height of the Cu substrate from the height-encoded map, following the same protocol as in our previous work.[46] The variations in the surface height of the Cu current collector are within the range of ±4 μm (Figure S10). Thus, we consider that our measurements of the "dead" Li height in this work are relatively robust. Although the height information obtained from PA imaging neglected the complex microstructures in the "dead" Li bulk (e.g., pore distribution), statistical analysis on the height distributions offered a direct

https://doi.org/10.1021/acsami.1c08944
ACS Appl. Mater. Interfaces 2021, 13, 35750−35758

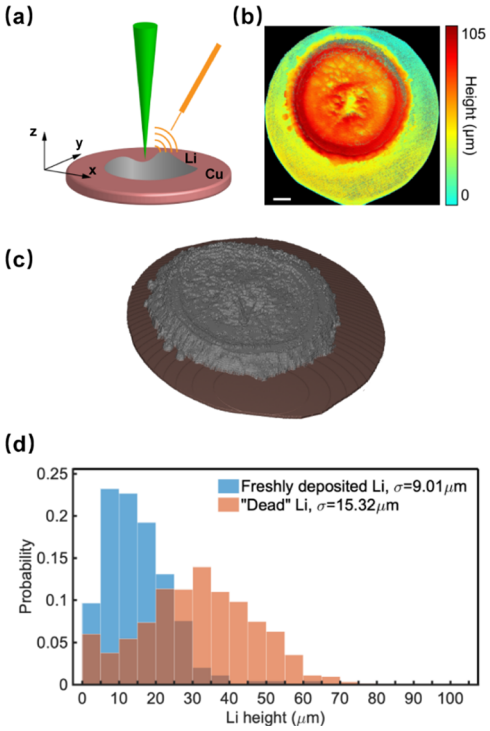

Figure 3. (a) Schematic illustration of the sample surface in a standard coordinate system under PA imaging. An $x-y$ height-encoded map is shown in (b) with a 1 mm scale bar. (c) 3D image of the "dead" Li on the Cu surface. (d) Height distribution of a 1.8 × 1.8 mm^2 region on freshly deposited Li (10 mA h cm^{-2}) and "dead" Li (approximately 10 mA h cm^{-2}).

comparison between the freshly deposited lithium metal and "dead" Li in terms of their topology. The average height of "dead" Li was calculated to be ∼39.76 μm, which is comparable to that of the freshly deposited Li. Significant height variance, however, was observed across the lithium surface, as shown in Figure 3c. Figure 3d shows the height distribution of freshly deposited Li and "dead" Li within a 1.8 × 1.8 mm^2 region selected from the central part of Li. The much more scattered distribution of the height of "dead" Li suggests that the heterogeneity of Li plating and stripping develops rather quickly with cycling.

DISCUSSION

Rates of Different Li-Loss Processes. Of the three routes of Li loss, the Li^0 loss due to "dead" Li formation dominated the total Li loss (more than 75%), and "dead" Li formation accelerated as cycling proceeded following a power function of $\sum\Delta Q = 0.00193t^{1.41}$. This phenomenon may be linked to the sudden "death" of Li-metal batteries commonly reported in the literature.[6,7] The total Li^+ loss rate is a constant (i.e., 0.00304 mA). It consists of two parts (SEI formation and galvanic corrosion), which occur concurrently during battery rest and cycling processes and share similar compositions. This makes it challenging to distinguish the rates of these two Li^+-loss processes. However, as discussed in the Introduction, the surface layer built upon "dead" Li, in principle, does not directly affect the charge-transfer resistance associated with the Li^+/Li redox reaction, whereas interphases generated in the Li^+-loss processes do. This provides us with an opportunity to follow the rate of different Li^+-loss processes in terms of Ω h^{-1} through impedance spectroscopy using a carefully designed cycling protocol. We note that this rate (Ω h^{-1}) is not yet directly comparable to the rate (mA) derived from GC and CE measurements.

EIS analysis was performed for a Li/Cu cell using the following cycling protocol to probe the rates of different Li^+-loss processes. The cell was rested for 12 h before cycling for 15 cycles (under 0.196 mA, 2 h discharge). During the rest process, the interphase grows both on Li metal, as a result of the chemical reaction between Li and the electrolyte (i.e., the chemically formed SEI), and on the Cu current collector as a result of galvanic corrosion. The resistance increase thus reflects these two processes of interphase growth. During the cycling process, Li is stripped from Li metal and deposits on the other side of the cell. The SEI continuously forms on the fresh Li metal surface through electrochemical reactions during cycling. In addition, the contact between Cu and the freshly deposited Li metal causes further galvanic corrosion in the cycling. As cycling proceeded, once the interphase layer on the

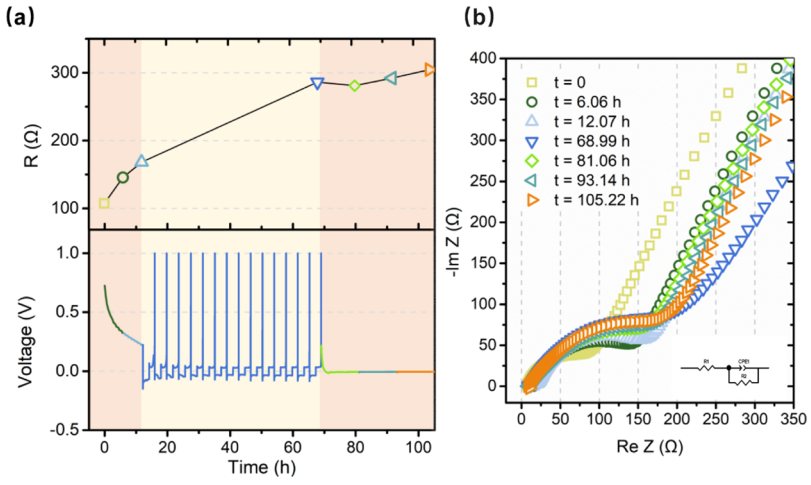

Figure 4. The calculated resistance and corresponding electrochemistry are shown in (a). The shaded area in pink corresponds to the rest process, and the shaded area in yellow corresponds to the cycling process. The impedance data are shown in (b), with the imaginary and real parts of the impedances shown on the y and x axes, respectively. The inset figure shows the equivalent circuit used for impedance fitting of the high-frequency arc. Through this fitting, the charge transfer resistance can be extracted.

https://doi.org/10.1021/acsami.1c08944
ACS Appl. Mater. Interfaces 2021, 13, 35750−35758

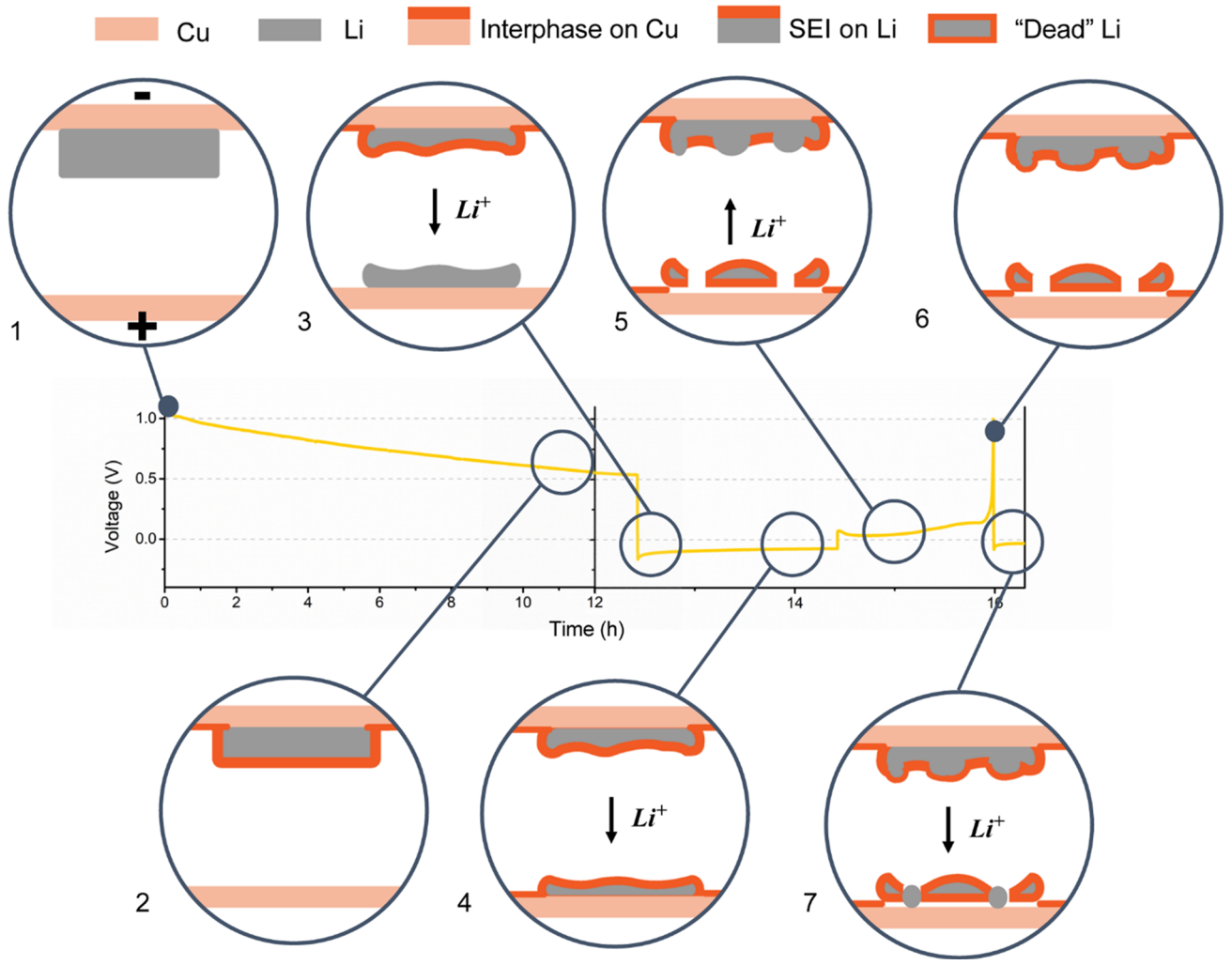

Figure 5. Interphase layer growth in a Li/Cu cell during rest and the initial cycles. State 1 to 2 shows the interphase that is formed on the Cu and lithium metal caused by galvanic corrosion and typical chemical SEI, respectively. State 3 shows the fresh lithium metal deposition on the positive Cu surface. From state 3 to state 4, the interphase is formed on the positive side through galvanic corrosion and electrochemical SEI formation. State 5 shows the formation of "dead" lithium and the fresh lithium metal protruded from the SEI layer on the negative side. From state 5 to 6, the SEI is formed on the freshly exposed lithium metal. State 7 shows lithium metal deposition on the positive side in a new discharge.

Cu surface was stabilized, the Li^+ loss was dominated by the electrochemical SEI. After 15 cycles, another rest of 36 h followed. During the second rest process, the Li^+ loss was dominated by the chemically formed SEI, where fresh lithium metal was again exposed to the liquid electrolyte. The impedance was measured every 4 h during the first rest, after cycling, and every 12 h during the second rest. The electrochemistry and calculated resistances are presented in Figure 4a (see Table S2 for fitting parameters). The EIS profile at each time point is shown in Figure 4b. The electrochemistry and EIS analysis of a similar cell without the second rest is presented in Figure S11 and Table S3 of the Supporting Information. From the EIS results, during cycling, the resistance growth rate is 2.07 Ω h^{-1}. In the first rest, the resistance first quickly increases to 168.20 Ω following a rate of 15.23 Ω h^{-1} in the first 4 h and then remains almost unchanged (also shown in Figure S11). In the second rest, the resistance growth is significantly slower (1.46 Ω h^{-1}).

On the basis of electrochemistry and the GC and EIS data, we now discuss the different Li loss processes and their rates (Figure 5). From state 1 (before cycling) to state 2 (toward the end of rest), the interphase layer grows both on the Li and Cu surfaces as a result of the chemically formed SEI and galvanic corrosion with a resistance growth rate of 15.23 Ω h^{-1}. State 3 to state 7 represent the interphase formation process (electrochemically formed SEI and galvanic corrosion process) together with possible "dead" Li formation both on the Li metal and the Cu current collector during cycling. For these states, the resistance growth rate is 2.07 Ω h^{-1}. In addition, the rate of the amount of Li^+ loss is 0.00304 mA, whereas the amount of "dead" Li grows following the power function ($\sum \Delta Q = 0.00193t^{1.41}$). If after one discharge and charge cycle, the cycling is stopped, then the resistance growth is attributed to the SEI formation on the newly exposed lithium-metal surface, similar to state 5 to 6 in Figure 5, with a rate of 1.46 Ω h^{-1}. This could explain the distinctly slow rate of resistance growth in the second rest period in Figure 4a, as most of the surface in the cell is already covered by the interphase layer. If the cycling continues, then Li metal is deposited on the positive Cu surface again, as shown in state 7 (Figure 5). The interphase layer grows during cycling following an iteration from state 4 to state 7.

Li Loss in Solid-State Cells. GC measurements were then extended to quantify Li loss in Li/Cu solid-state cells with an

https://doi.org/10.1021/acsami.1c08944
ACS Appl. Mater. Interfaces 2021, 13, 35750−35758

LGPS solid-state electrolyte (Figure S5). The cell was rested for 12 h before cycling at a current density of 0.1 mA. From the electrochemistry, as shown in Figure 6a,b, almost no lithium

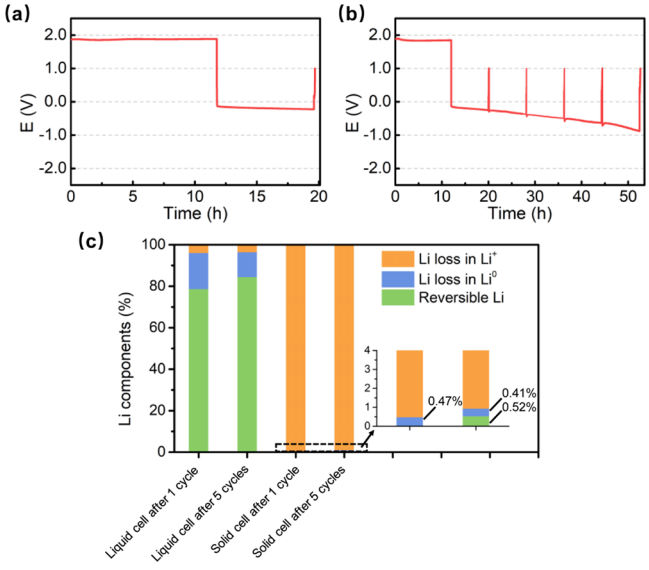

Figure 6. Electrochemistry of Li/LGPS/Cu solid-state cell cycles for (a) one and (b) five times. These cells were used in the GC tests. (c) Different Li components (in percentages) for liquid Li/Cu cells after 1 and 5 cycles and for solid-state Li/Cu cells with an LGPS electrolyte after 1 and 5 cycles. The inset shows a zoom-in of the black-dashed region.

stripping was observed in the first 5 cycles, thus close to 100% Li loss, while Li "plating" always occurred. As previous simulation and experimental works have shown that LGPS is not thermodynamically stable against a Li metal forming mixed conducting interphase,[51−56] this suggests that Li can be lost in Li^+ due to interphase formation and/or in Li^0 due to the loss of physical contact between Li and LGPS or the current collector. The GC measurements as shown in Figure 6c revealed that over 99% of the Li loss in the Li/LGPS/Cu solid-state cells was due to interphase formation and thus Li^+ loss (Li^0 loss contributes only 0.4%), in stark contrast to that in liquid cells, where Li^0 loss dominated. Limited improvement of the lithium metal reversibility was observed with longer cycles (Figure S4), as evidenced by the more profound stripping behavior. For a Li/LGPS/Li symmetric cell, where an excess amount of Li metal is provided at both ends, such behavior would be masked by "normal" plating and stripping electrochemistry. Therefore, testing with a Li/Cu asymmetric cell is clearly much more informative. The remaining question, however, is whether the Li^+ loss is only caused by reactions between Li metal and LGPS or whether a similar galvanic corrosion process also exists. Cracks can also affect the Li plating and stripping processes. During cycling, cracks can form at the surface of a solid electrolyte due to volume expansion of electrodes.[57] These cracks prohibit Li ion transport at the interface and hence increase interfacial resistance.

CONCLUSIONS

We observed that the Li loss in Li/Cu half-cells with a $LiPF_6$-carbonate electrolyte is dominated by "dead" Li formation (Li^0 loss). The Li^0 loss was observed to accelerate as cycling proceeded. Furthermore, PA imaging was used to examine the 3D morphology of "dead" Li, indicating that heterogeneity of Li plating and stripping develops quickly during the first tens of cycles. By combining GC and EIS measurements, the Li loss rates of different processes (SEI, galvanic corrosion, and "dead" Li) were also quantified. Finally, GC analysis on Li/LGPS/Cu solid-state cells revealed that interphase formation consumed almost all of the lithium metal (more than 99%), leading to no Li stripping during charging. This finding indicates that the interface reaction between Li and LGPS is extremely severe. However, such a behavior can be masked in a Li/Li symmetric cell. We thus suggest the use of Li/Cu asymmetric cells in the evaluation of compatibility between Li and solid-state electrolytes in future studies. Overall, our work quantified the rates of different Li loss processes in Li-metal batteries, which is extremely important for battery life prognosis and battery design. Our work, together with several recent reports of other groups, further highlights the importance of quantitative studies in Li-metal and solid-state batteries.

ASSOCIATED CONTENT

Supporting Information

The Supporting Information is available free of charge at https://pubs.acs.org/doi/10.1021/acsami.1c08944.

Electrochemistry of the cycling and CE profiles of the cells; GC experimental data for the liquid cell and the GC peak for the solid-state cell; concept diagram for the PA system and the sample stage; resolution calibration for PA imaging; Cu surface profile inspection by PA imaging; EIS data analysis (PDF)

AUTHOR INFORMATION

Corresponding Author

Shou-Hang Bo − *University of Michigan-Shanghai Jiao Tong University Joint Institute, Shanghai Jiao Tong University, Shanghai 200240, China;* orcid.org/0000-0001-8963-5261; Email: shouhang.bo@sjtu.edu.cn

Authors

Yibo Zhao − *University of Michigan-Shanghai Jiao Tong University Joint Institute, Shanghai Jiao Tong University, Shanghai 200240, China;* orcid.org/0000-0003-1437-3767

Yifan Wu − *University of Michigan-Shanghai Jiao Tong University Joint Institute, Shanghai Jiao Tong University, Shanghai 200240, China*

Huihui Liu − *University of Michigan-Shanghai Jiao Tong University Joint Institute, Shanghai Jiao Tong University, Shanghai 200240, China*

Sung-Liang Chen − *University of Michigan-Shanghai Jiao Tong University Joint Institute, Shanghai Jiao Tong University, Shanghai 200240, China;* orcid.org/0000-0002-0572-5110

Complete contact information is available at: https://pubs.acs.org/10.1021/acsami.1c08944

Author Contributions

‡Y.Z. and Y.W. contributed equally. The manuscript was written through contributions of all authors. All authors have given approval to the final version of the manuscript.

Notes

The authors declare no competing financial interest.

■ ACKNOWLEDGMENTS

The authors acknowledge support from the Shanghai Sailing program (18YF1411100).

■ REFERENCES

(1) Xu, W.; Wang, J.; Ding, F.; Chen, X.; Nasybulin, E.; Zhang, Y.; Zhang, J.-G. Lithium Metal Anodes for Rechargeable Batteries. *Energy Environ. Sci.* **2014**, *7*, 513−537.

(2) Xiao, J.; Li, Q.; Bi, Y.; Cai, M.; Dunn, B.; Glossmann, T.; Liu, J.; Osaka, T.; Sugiura, R.; Wu, B.; Yang, J.; Zhang, J.-G.; Whittingham, M. S. Understanding and Applying Coulombic Efficiency in Lithium Metal Batteries. *Nat. Energy* **2020**, *5*, 561−568.

(3) Weber, R.; Genovese, M.; Louli, A. J.; Hames, S.; Martin, C.; Hill, I. G.; Dahn, J. R. Long Cycle Life and Dendrite-Free Lithium Morphology in Anode-Free Lithium Pouch Cells Enabled by a Dual-Salt Liquid Electrolyte. *Nat. Energy* **2019**, *4*, 683−689.

(4) Ministry of Industry and Information Technology of the People's Republic of China. Cycle Life Requirements and Test Methods for Traction Battery of Electric Vehicle. GB/T 31484−2015. http://c.gb688.cn/bzgk/gb/showGb?type=online&hcno=44ECF0443BD82A81A512FB05092677EE, 2015.

(5) Adams, B. D.; Zheng, J.; Ren, X.; Xu, W.; Zhang, J.-G. Accurate Determination of Coulombic Efficiency for Lithium Metal Anodes and Lithium Metal Batteries. *Adv. Energy Mater.* **2018**, *8*, 1702097.

(6) Lu, D.; Shao, Y.; Lozano, T.; Bennett, W. D.; Graff, G. L.; Polzin, B.; Zhang, J.; Engelhard, M. H.; Saenz, N. T.; Henderson, W. A.; Bhattacharya, P.; Liu, J.; Xiao, J. Failure Mechanism for Fast-Charged Lithium Metal Batteries with Liquid Electrolytes. *Adv. Energy Mater.* **2015**, *5*, 1400993.

(7) Niu, C.; Lee, H.; Chen, S.; Li, Q.; Du, J.; Xu, W.; Zhang, J.-G.; Whittingham, M. S.; Xiao, J.; Liu, J. High-Energy Lithium Metal Pouch Cells with Limited Anode Swelling and Long Stable Cycles. *Nat. Energy* **2019**, *4*, 551−559.

(8) Chen, S.; Niu, C.; Lee, H.; Li, Q.; Yu, L.; Xu, W.; Zhang, J.-G.; Dufek, E. J.; Whittingham, M. S.; Meng, S.; Xiao, J.; Liu, J. Critical Parameters for Evaluating Coin Cells and Pouch Cells of Rechargeable Li-Metal Batteries. *Joule* **2019**, *3*, 1094−1105.

(9) Cheng, X.-B.; Zhang, R.; Zhao, C.-Z.; Zhang, Q. Toward Safe Lithium Metal Anode in Rechargeable Batteries: A Review. *Chem. Rev.* **2017**, *117*, 10403−10473.

(10) Albertus, P.; Babinec, S.; Litzelman, S.; Newman, A. Status and Challenges in Enabling the Lithium Metal Electrode for High-Energy and Low-Cost Rechargeable Batteries. *Nat. Energy* **2018**, *3*, 16−21.

(11) Smith, A. J.; Burns, J. C.; Zhao, X.; Xiong, D.; Dahn, J. R. A High Precision Coulometry Study of the SEI Growth in Li/Graphite Cells. *J. Electrochem. Soc.* **2011**, *158*, A447.

(12) Attia, P. M.; Das, S.; Harris, S. J.; Bazant, M. Z.; Chueh, W. C. Electrochemical Kinetics of SEI Growth on Carbon Black: Part I. Experiments. *J. Electrochem. Soc.* **2019**, *166*, E97−E106.

(13) Yoshimatsu, I.; Hirai, T.; Yamaki, J. I. Lithium Electrode Morphology During Cycling in Lithium Cells. *J. Electrochem. Soc.* **1988**, *135*, 2422−2427.

(14) Wood, K. N.; Kazyak, E.; Chadwick, A. F.; Chen, K.-H.; Zhang, J.-G.; Thornton, K.; Dasgupta, N. P. Dendrites and Pits: Untangling the Complex Behavior of Lithium Metal Anodes through Operando Video Microscopy. *ACS Cent. Sci.* **2016**, *2*, 790−801.

(15) Wood, K. N.; Noked, M.; Dasgupta, N. P. Lithium Metal Anodes: Toward an Improved Understanding of Coupled Morphological, Electrochemical, and Mechanical Behavior. *ACS Energy Lett.* **2017**, *2*, 664−672.

(16) Chen, K.-H.; Wood, K. N.; Kazyak, E.; LePage, W. S.; Davis, A. L.; Sanchez, A. J.; Dasgupta, N. P. Dead Lithium: Mass Transport Effects on Voltage, Capacity, and Failure of Lithium Metal Anodes. *J. Mater. Chem. A* **2017**, *5*, 11671−11681.

(17) Lin, D.; Liu, Y.; Li, Y.; Li, Y.; Pei, A.; Xie, J.; Huang, W.; Cui, Y. Fast Galvanic Lithium Corrosion Involving a Kirkendall-Type Mechanism. *Nat. Chem.* **2019**, *11*, 382−389.

(18) Kolesnikov, A.; Kolek, M.; Dohmann, J. F.; Horsthemke, F.; Börner, M.; Bieker, P.; Winter, M.; Stan, M. C. Galvanic Corrosion of Lithium-Powder-Based Electrodes. *Adv. Energy Mater.* **2020**, *10*, 2000017.

(19) Kazyak, E.; Garcia-Mendez, R.; LePage, W. S.; Sharafi, A.; Davis, A. L.; Sanchez, A. J.; Chen, K.-H.; Haslam, C.; Sakamoto, J.; Dasgupta, N. P. Li Penetration in Ceramic Solid Electrolytes: Operando Microscopy Analysis of Morphology, Propagation, and Reversibility. *Matter* **2020**, *2*, 1025−1048.

(20) Cheng, X.-B.; Zhang, R.; Zhao, C.-Z.; Wei, F.; Zhang, J.-G.; Zhang, Q. A Review of Solid Electrolyte Interphases on Lithium Metal Anode. *Adv. Sci.* **2016**, *3*, 1500213.

(21) Peled, E. The Electrochemical Behavior of Alkali and Alkaline Earth Metals in Nonaqueous Battery Systems—the Solid Electrolyte Interphase Model. *J. Electrochem. Soc.* **1979**, *126*, 2047−2051.

(22) Qian, J.; Henderson, W. A.; Xu, W.; Bhattacharya, P.; Engelhard, M.; Borodin, O.; Zhang, J.-G. High Rate and Stable Cycling of Lithium Metal Anode. *Nat. Commun.* **2015**, *6*, 6362.

(23) Schmitz, R.; Ansgar Müller, R.; Wilhelm Schmitz, R.; Schreiner, C.; Kunze, M.; Lex-Balducci, A.; Passerini, S.; Winter, M. SEI Investigations on Copper Electrodes after Lithium Plating with Raman Spectroscopy and Mass Spectrometry. *J. Power Sources* **2013**, *233*, 110−114.

(24) Aurbach, D.; Gofer, Y.; Langzam, J. The Correlation between Surface Chemistry, Surface Morphology, and Cycling Efficiency of Lithium Electrodes in a Few Polar Aprotic Systems. *J. Electrochem. Soc.* **1989**, *136*, 3198−3205.

(25) Aurbach, D.; Ein-Ely, Y.; Zaban, A. The Surface Chemistry of Lithium Electrodes in Alkyl Carbonate Solutions. *J. Electrochem. Soc.* **1994**, *141*, L1−L3.

(26) Lu, Y.; Tu, Z.; Archer, L. A. Stable Lithium Electrodeposition in Liquid and Nanoporous Solid Electrolytes. *Nat. Mater.* **2014**, *13*, 961−969.

(27) Aurbach, D. Review of Selected Electrode−Solution Interactions Which Determine the Performance of Li and Li Ion Batteries. *J. Power Sources* **2000**, *89*, 206−218.

(28) Peled, E.; Golodnitsky, D.; Ardel, G. Advanced Model for Solid Electrolyte Interphase Electrodes in Liquid and Polymer Electrolytes. *J. Electrochem. Soc.* **1997**, *144*, L208−L210.

(29) Li, Y.; Li, Y.; Pei, A.; Yan, K.; Sun, Y.; Wu, C.-L.; Joubert, L.-M.; Chin, R.; Koh, A. L.; Yu, Y.; Perrino, J.; Butz, B.; Chu, S.; Cui, Y. Atomic Structure of Sensitive Battery Materials and Interfaces Revealed by Cryo−Electron Microscopy. *Science* **2017**, *358*, 506.

(30) Wang, X.; Zhang, M.; Alvarado, J.; Wang, S.; Sina, M.; Lu, B.; Bouwer, J.; Xu, W.; Xiao, J.; Zhang, J.-G.; Liu, J.; Meng, Y. S. New Insights on the Structure of Electrochemically Deposited Lithium Metal and Its Solid Electrolyte Interphases Via Cryogenic TEM. *Nano Lett.* **2017**, *17*, 7606−7612.

(31) Huang, W.; Boyle, D. T.; Li, Y.; Li, Y.; Pei, A.; Chen, H.; Cui, Y. Nanostructural and Electrochemical Evolution of the Solid-Electrolyte Interphase on CuO Nanowires Revealed by Cryogenic-Electron Microscopy and Impedance Spectroscopy. *ACS Nano* **2019**, *13*, 737−744.

(32) Fei, Z.; Kelly, R. G.; Hudson, J. L. Spatiotemporal Patterns on Electrode Arrays. *J. Phys. Chem.* **1996**, *100*, 18986−18991.

(33) Yang, L.; Yang, A. A. Communication—on Zero-Resistance Ammeter and Zero-Voltage Ammeter. *J. Electrochem. Soc.* **2017**, *164*, C819−C821.

(34) Aryanfar, A.; Brooks, D. J.; Colussi, A. J.; Hoffmann, M. R. Quantifying the Dependence of Dead Lithium Losses on the Cycling Period in Lithium Metal Batteries. *Phys. Chem. Chem. Phys.* **2014**, *16*, 24965−24970.

(35) Sanchez, A. J.; Kazyak, E.; Chen, Y.; Chen, K.-H.; Pattison, E. R.; Dasgupta, N. P. Plan-view operando video microscopy of Li metal anodes: identifying the coupled relationships among nucleation, morphology, and reversibility. *ACS Energy Lett.* **2020**, *5*, 994−1004.

(36) Tewari, D.; Rangarajan, S. P.; Balbuena, P. B.; Barsukov, Y.; Mukherjee, P. P. Mesoscale Anatomy of Dead Lithium Formation. *J. Phys. Chem. C* **2020**, *124*, 6502−6511.

(37) Sheng, S.-E.; Sheng, L.; Wang, L.; Piao, N.; He, X. Thickness Variation of Lithium Metal Anode with Cycling. *J. Power Sources* **2020**, *476*, 228749.
(38) Fang, C.; Li, J.; Zhang, M.; Zhang, Y.; Yang, F.; Lee, J. Z.; Lee, M.-H.; Alvarado, J.; Schroeder, M. A.; Yang, Y.; Lu, B.; Williams, N.; Ceja, M.; Yang, L.; Cai, M.; Gu, J.; Xu, K.; Wang, X.; Meng, Y. S. Quantifying Inactive Lithium in Lithium Metal Batteries. *Nature* **2019**, *572*, 511−515.
(39) Metzger, M.; Strehle, B.; Solchenbach, S.; Gasteiger, H. A. Origin of H_2 Evolution in LIBs: H_2O Reduction vs. Electrolyte Oxidation. *J. Electrochem. Soc.* **2016**, *163*, A798−A809.
(40) Xu, G.; Li, J.; Wang, C.; Du, X.; Lu, D.; Xie, B.; Wang, X.; Lu, C.; Liu, H.; Dong, S.; Cui, G.; Chen, L. The Formation/Decomposition Equilibrium of LiH and Its Contribution on Anode Failure in Practical Lithium Metal Batteries. *Angew. Chem., Int. Ed.* **2021**, *60*, 7770−7776.
(41) McShane, E. J.; Colclasure, A. M.; Brown, D. E.; Konz, Z. M.; Smith, K.; McCloskey, B. D. Quantification of Inactive Lithium and Solid−Electrolyte Interphase Species on Graphite Electrodes after Fast Charging. *ACS Energy Lett.* **2020**, *5*, 2045−2051.
(42) Gunnarsdóttir, A. B.; Amanchukwu, C. V.; Menkin, S.; Grey, C. P. Noninvasive In Situ NMR Study of "Dead Lithium" Formation and Lithium Corrosion in Full-Cell Lithium Metal Batteries. *J. Am. Chem. Soc.* **2020**, *142*, 20814−20827.
(43) Xiang, Y.; Zhong, G.; Tao, M.; Liang, Z.; Zheng, G.; Liu, X.; Jin, Y.; Armand, M.; Zhang, J.-G.; Xu, K.; Fu, R.; Yang, Y., Operando Tracing and Quantifying Inactive Li in Lithium Metal Battery. Xiamen University: ChemRxiv, 2020. DOI: 10.26434/chemrxiv.12910259.v1.
(44) Hsieh, Y.-C.; Leißing, M.; Nowak, S.; Hwang, B.-J.; Winter, M.; Brunklaus, G. Quantification of Dead Lithium Via *In Situ* Nuclear Magnetic Resonance Spectroscopy. *Cell Rep. Phys. Sci.* **2020**, *1*, 100139.
(45) Liu, H.; Zhao, Y.; Zhou, J.; Li, P.; Bo, S.-H.; Chen, S.-L. Photoacoustic Imaging of Lithium Metal Batteries. *ACS Appl. Energy Mater.* **2020**, *3*, 1260−1264.
(46) Huihui, L.; Yibo, Z.; Shou-Hang, B.; Sung-Liang, C. In *Application of Photoacoustic Imaging for Lithium Metal Batteries*, Proc.SPIE, On-line, On-line, 2020; p 115490U.
(47) Yao, J.; Wang, L. V. Photoacoustic Microscopy. *Laser Photonics Rev.* **2013**, *7*, 758−778.
(48) Attia, P. M.; Chueh, W. C.; Harris, S. J. Revisiting the $t^{0.5}$ Dependence of SEI Growth. *J. Electrochem. Soc.* **2020**, *167*, 090535.
(49) von Kolzenberg, L.; Latz, A.; Horstmann, B. Solid−Electrolyte Interphase During Battery Cycling: Theory of Growth Regimes. *ChemSusChem* **2020**, *13*, 3901−3910.
(50) Shadike, Z.; Lee, H.; Borodin, O.; Cao, X.; Fan, X.; Wang, X.; Lin, R.; Bak, S.-M.; Ghose, S.; Xu, K.; Wang, C.; Liu, J.; Xiao, J.; Yang, X.-Q.; Hu, E. Identification of LiH and Nanocrystalline LiF in the Solid−Electrolyte Interphase of Lithium Metal Anodes. *Nat. Nanotechnol.* **2021**, *16*, 549−554.
(51) Han, F.; Zhu, Y.; He, X.; Mo, Y.; Wang, C. Electrochemical Stability of $Li_{10}GeP_2S_{12}$ and $Li_7La_3Zr_2O_{12}$ Solid Electrolytes. *Adv. Energy Mater.* **2016**, *6*, 1501590.
(52) Sun, Y.; Yan, W.; An, L.; Wu, B.; Zhong, K.; Yang, R. A Facile Strategy to Improve the Electrochemical Stability of a Lithium Ion Conducting $Li_{10}GeP_2S_{12}$ Solid Electrolyte. *Solid State Ionics* **2017**, *301*, 59−63.
(53) Camacho-Forero, L. E.; Balbuena, P. B. Exploring Interfacial Stability of Solid-State Electrolytes at the Lithium-Metal Anode Surface. *J. Power Sources* **2018**, *396*, 782−790.
(54) Richards, W. D.; Miara, L. J.; Wang, Y.; Kim, J. C.; Ceder, G. Interface Stability in Solid-State Batteries. *Chem. Mater.* **2016**, *28*, 266−273.
(55) Wenzel, S.; Randau, S.; Leichtweiß, T.; Weber, D. A.; Sann, J.; Zeier, W. G.; Janek, J. Direct Observation of the Interfacial Instability of the Fast Ionic Conductor $Li_{10}GeP_2S_{12}$ at the Lithium Metal Anode. *Chem. Mater.* **2016**, *28*, 2400−2407.
(56) Xiao, Y.; Wang, Y.; Bo, S.-H.; Kim, J. C.; Miara, L. J.; Ceder, G. Understanding Interface Stability in Solid-State Batteries. *Nat. Rev. Mater.* **2020**, *5*, 105−126.
(57) Ning, Z.; Jolly, D. S.; Li, G.; De Meyere, R.; Pu, S. D.; Chen, Y.; Kasemchainan, J.; Ihli, J.; Gong, C.; Liu, B.; Melvin, D. L. R.; Bonnin, A.; Magdysyuk, O.; Adamson, P.; Hartley, G. O.; Monroe, C. W.; Marrow, T. J.; Bruce, P. G. Visualizing Plating-Induced Cracking in Lithium-Anode Solid-Electrolyte Cells. *Nat. Mater.* **2021**, DOI: 10.5287/bodleian:9Rn6n6o15.